



**HAL**  
open science

## Lagrangian-based Simulations of Hypervelocity Impact Experiments on Mars Regolith Proxy

M. Froment, E. Rougier, C. Larmat, Z. Lei, B. Euser, S. Kedar, J. E  
Richardson, T. Kawamura, P. Lognonné

► **To cite this version:**

M. Froment, E. Rougier, C. Larmat, Z. Lei, B. Euser, et al.. Lagrangian-based Simulations of Hypervelocity Impact Experiments on Mars Regolith Proxy. *Geophysical Research Letters*, 2020, 47 (13), pp.e2020GL087393. 10.1029/2020GL087393 . hal-02975098

**HAL Id: hal-02975098**

**<https://hal.science/hal-02975098v1>**

Submitted on 22 Oct 2020

**HAL** is a multi-disciplinary open access archive for the deposit and dissemination of scientific research documents, whether they are published or not. The documents may come from teaching and research institutions in France or abroad, or from public or private research centers.

L'archive ouverte pluridisciplinaire **HAL**, est destinée au dépôt et à la diffusion de documents scientifiques de niveau recherche, publiés ou non, émanant des établissements d'enseignement et de recherche français ou étrangers, des laboratoires publics ou privés.

# Lagrangian-based simulations of hypervelocity impact experiments on Mars regolith proxy

M. Froment<sup>1,2</sup>, E. Rougier<sup>2</sup>, C. Larmat<sup>2</sup>, Z. Lei<sup>2</sup>, B. Euser<sup>2</sup>, S. Kedar<sup>4</sup>, J. E. Richardson<sup>3</sup>, T. Kawamura<sup>5</sup>, and P. Lognonné<sup>5</sup>

<sup>1</sup>École Normale Supérieure Paris-Saclay, Cachan, France

<sup>2</sup>Earth and Environmental Division, Los Alamos National Laboratory, New Mexico, USA

<sup>3</sup>Planetary Science Institute, Tucson, Arizona, USA

<sup>4</sup>Jet Propulsion Laboratory, California Institute of Technology, Pasadena, California, USA <sup>5</sup>Université de Paris, Institut de physique du globe de Paris, CNRS, F-75005 Paris, France

## Key Points:

- We conduct a parametric study of a novel Lagrangian numerical model of shock waves in granular media, with application to Mars regolith.
- We validate this model with a laboratory experiment in pumice sand with an impact velocity of 0.98 km/s.
- Amplitude of shock waves and transition to different regimes is explained by the model for the sensors placed vertically from the impact.

17

18

## Abstract

19

Most of the surface of Mars is covered with unconsolidated rocky material, known as re-golith.

20

High-fidelity models of the dynamics of impacts in such material are needed to help with the interpretation of seismic signals that are now recorded by SEIS, the seis-mometer of InSight.

21

22

We developed a numerical model for impacts on regolith, using the novel Hybrid Optimization Software Suite (HOSS) which is a Lagrangian code mixing finite and discrete element formulations. We use data from hypervelocity impact experiments performed on pumice sand at the NASA Ames Vertical Gun Range to identify and calibrate key model parameters. The model provides insight into the plastic-elastic transition observed in the data and it also demonstrates that gravity plays a key role in the material response. Waveforms for receivers situated vertically below the impact point are correctly modeled, while more research is needed to explain the shallow receivers' signals.

23

24

25

26

27

28

29

30

## Plain Language Summary

31

The generation of seismic waves by meteorite impacts in unconsolidated materials, such as Mars regolith, is a complex dynamic process. We present a numerical model based on a novel method and show its potential to explain the main characteristics of shock and seismic waves generated by impacts at laboratory scales. Our goal is to use this model to help with the analysis of data recorded during the InSight mission.

32

33

34

35

36

## 1 Introduction

37

InSight landed on Mars on November 26, 2018. Since then, the lander's robotic arm has placed a seismometer, the SEIS experiment, for the first time on the direct surface of the planet (Lognonné et al., 2019). SEIS is a single seismic station completed by pressure and wind sensors (Banfield et al., 2019). The absence of other stations to form a network can make the assessment of source distance and azimuth sometimes challenging based on the first SEIS observations (Lognonné et al., 2020; Giardini et al., 2020). Being able to identify signals produced by impacts would thus prove relevant to the mission, as fresh craters can potentially be located by satellite imagery and provide a strong constraint on the source position (Daubar et al., 2018). Current estimations and measures of impact rates on Mars show a higher frequency of craters smaller than 10m diameter, with 10 times more craters in the range of [3.9, 5.5] m diameter created every

38

39

40

41

42

43

44

45

46

47

48 year compared to craters of [11, 15.6] m diameter (Teanby, 2015; Daubar et al., 2013; Ma-  
49 lin et al., 2006). The expected rate of detection is estimated to about 8 impacts per year  
50 for the SEIS VBB (Banerdt et al., 2020), close to the pre-launch proposed rate (Lognonné  
51 & Johnson, 2007; Daubar et al., 2018). The generation of seismic signals by such small  
52 events is dominated by the response of Mars regolith, a layer of unconsolidated rocky  
53 material covering the bedrock, which is supposedly desiccated at the InSight landing site  
54 close to Mars equator (Morgan et al., 2018). First analyses have confirmed low seismic  
55 velocities, which might even be as low as 120 m/s for P waves at 0.5 m depth (Lognonné  
56 et al., 2020). Physic-based shock propagation codes allow high-fidelity modeling of the  
57 shock waves generated by meteorite impacts, which transition to seismic waves at fur-  
58 ther distances and thus control the shape and amplitude of the seismic signal that could  
59 be recorded by SEIS. Such modeling requires the codes to be able to track discontinu-  
60 ous features in time and space, like material fractures and phase transitions caused by  
61 the shock. Moreover, small impacts are expected to happen mostly in a solid regime of  
62 high viscosity, making the capture of non-isotropic processes an important requirement  
63 for simulation softwares.

64 Another challenge of modeling impacts in Mars regolith is its granular nature: fric-  
65 tion and grain displacement processes in the material are important and grain interac-  
66 tion can lead to non-linear behaviors that manifest as “force-chains” (Sun et al., 2009;  
67 Gao et al., 2019) and “fairy-castle” structures (Hapke & van Hoen, 1963; Carrier et al.,  
68 1991) depending on the confining stress on the grains. Moreover, the material is porous,  
69 which leads to an enhanced attenuation of shocks compared to bulk materials (Collins  
70 et al., 2019). Only now numerical methods to model impacts are starting to implement  
71 realistic, geologic materials as their target (Güldemeister & Wünnemann, 2017; Pierazzo  
72 et al., 2008; Wünnemann et al., 2006). Here, we use the novel Lagrangian mechanical  
73 software HOSS, based on a finite-discrete element formulation (Munjiza, 2004; Munjiza  
74 et al., 2011, 2014, 2013; Lei et al., 2014), to create a new numerical model of impacts in  
75 regolith. The lagrangian framework is appropriately tackling all modeling challenges stated  
76 above, as it allows for a straightforward description of discontinuities in unconsolidated  
77 materials and deviatoric stresses. Consequently, a better description of shear waves and  
78 surface processes is possible as well as non-isotropic impact processes.

79 In the following, we present the laboratory experiments we use to validate the nu-  
80 merical model, as well as the numerical method and the material model used to describe

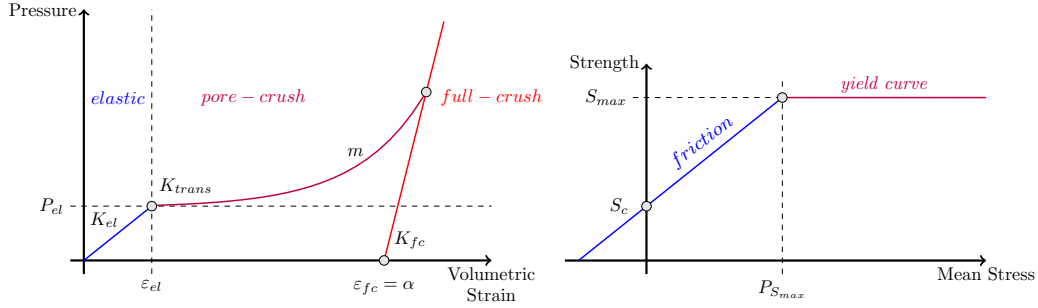


**Figure 1.** Simplified representation of the Equation of State (left) and the Strength Equation (right) and their key parameters.

81 Mars regolith. We present results of a parametric study of the model where we identify  
 82 which parameters control the transition to the different regimes of impacts, meaning from  
 83 shock to plastic to elastic response of the material. We then present a comparison of the  
 84 model predictions to the laboratory data, before finishing with discussions and conclu-  
 85 sions.

## 86 2 Laboratory experiments and model.

### 87 2.1 Experiments

88 The validation of the novel numerical model presented in this paper is done with  
 89 data from a series of laboratory impact experiments conducted at the NASA/AVGR fa-  
 90 cility (Richardson & Kedar, 2013). The experimental setup is composed of a cylindri-  
 91 cal tank, 1 meter in radius and in height, filled with a target bed and placed inside a cham-  
 92 ber with a controlled atmosphere. Tests were monitored by 15 accelerometers buried into  
 93 the target at different positions. Sampling rate is  $10^{-5}$  s.

94 We focus on two experiments performed in an Earth atmosphere at Martian pres-  
 95 sure of 5 to 10 torr, and on a target bed of pumice sand. This sand has a grain size of  
 96 0.1 to 0.2 mm, a porosity of 62%, and a composition and density similar to the John-  
 97 son Space Center (JSC) Mars-1 Regolith Simulant (Allen et al., 1997). In this study, the  
 98 impactor is a 6.3 mm diameter bead with a mass of 0.29g made of Pyrex, and an impact  
 99 velocity of 0.98 km/s.

## 2.2 Numerical model

The numerical model is based on a finite-discrete element representation (FDEM) used to handle the unconsolidated nature of Mars regolith. FDEM merges continuum solutions for the calculation of stresses as a function of deformation with the discrete element method for the resolution of fracture, fragmentation and contact interaction (Munjiza, 2004; Munjiza et al., 2011, 2014, 2013; Lei et al., 2014; Lei, Rougier, Knight, Munjiza, & Viswanathan, 2016; Lei, Rougier, Knight, Frash, et al., 2016).

We generate meshes of tetrahedral elements covering a 30° sector of the experiment tank. The numerical volume is 90cm deep and wide and contains around 1,000,000 elements. Each Lagrangian finite element (FE) contains from approximately 1000 grains of sand for the smallest ones close to the impactor (tetrahedrons of 1mm edges) and 1,000,000 grains of sand for the largest ones (tetrahedrons of 1cm edges), allowing for a mesoscale representation of the sand properties.

To simulate the grain displacements involved in impacts in unconsolidated material, HOSS treats the tetrahedral FEs as an unconsolidated heap where the elements interact only through frictional contact, with a Coulomb coefficient of friction of 0.75 for this study. Inside each FE, the material model is governed by two equations, depicted in Figure 1. One describes the volumetric response, or Equation of State (EOS), and the other the deviatoric response, or Strength Equation (SE). The EOS is a function of pressure with volumetric strain and has three different domains. The first one is elastic, with pressure increasing linearly with strain, given a bulk modulus  $K_{el}$ , as  $P(\varepsilon) = K_{el}\varepsilon$ . After a limit pressure  $P_{el}$  is reached, the porous material undergoes grain displacement and grain crushing. This domain starts with a break of slope from  $K_{el}$  to  $K_{trans}$  and is followed by an exponential increase of pressure with deformation. The equation of this curve is :

$$P(\varepsilon) = P_{el} + \frac{K_{trans}}{m \cdot \ln(10)} (10^{m(\varepsilon - \varepsilon_{el})} - 1) \quad \text{for} \quad \varepsilon \geq \varepsilon_{el}. \quad (1)$$

where  $\varepsilon$  is the strain,  $\varepsilon_{el}$  is the upper strain limit of the elastic regime and  $m$  is a parameter describing the exponent of the curve.  $K_{trans}$  drives the slope of the pore-crush curve at the beginning of the crushing processes. Given two values of  $K_{trans}$ , a lower value means that the material is easier to crush, because a lower amount of pressure is sufficient to obtain the same amount of deformation as with a higher value.  $m$  is the expo-

130 nent of the pore-crush curve and the same reasoning applies, i.e., a low  $m$  results in an  
131 easily crushable material.

132 Finally, when the material is fully crushed and all the porosity  $\alpha$  of the material  
133 disappears, the exponential curve morphs into a straight line with bulk modulus  $K_{fc}$  of  
134 a non-porous rock of the same composition.

135 The SE (Figure 1, right) sets the limit deviatoric stress (i.e., yield stress) that can  
136 be sustained by the material for any given mean stress. In this simplified model, the yield  
137 curve first increases linearly with mean stress and upon reaching the yield limit ( $P_{S_{max}}, S_{max}$ ),  
138 it becomes constant, transitioning to a more viscous behavior. In the case of a granu-  
139 lar material like sand, the cohesion  $S_c$  of the material is zero.

140 The response of the impactor’s material is represented using the Munjiza’s elas-  
141 tic model (Munjiza et al., 2014; Lei, Rougier, Knight, Frash, et al., 2016). The FE size  
142 and impact speed result in an integration time step of a few nanoseconds. Given the time  
143 scale of the experimental signals, the simulation need to be run up to a few milliseconds.

## 144 **3 Results**

### 145 **3.1 Parametric study**

146 This work focuses on the parameters  $K_{el}$ ,  $K_{trans}$ ,  $m$ ,  $P_{el}$  and  $P_{S_{max}}$ . For each of  
147 these parameters, between 3 and 4 simulations are run to explore the effect of their change  
148 on the shock wave properties. This first set of analysis is conducted without including  
149 Earth gravity to the simulation. The effects of this additional force are discussed in sec-  
150 tion 3.2.

151 Literature on sand mechanical properties provide ranges of values for some of these  
152 parameters. The parameter  $m$  thus seems to be between 3 and 6 for the sand studied  
153 in (Luo et al., 2011; Yamamuro et al., 1996, 2011). The elastic p-wave velocities mea-  
154 sured on Mars regolith simulants (Morgan et al., 2018) range between 80 m/s and 250  
155 m/s and the Poisson’s ratio is around 0.2, leading to  $K_{el}$  roughly between 5MPa and 60MPa  
156 for a bulk density of 880 kg/m<sup>3</sup>. In many experiments (Berney IV & Smith, 2008; Hy-  
157 odo et al., 2002), the shear response of sands tends to remain in the domain of Coulomb  
158 friction even above a few MPa of pressure, leading to  $P_{S_{max}} > 10^6$  Pa.

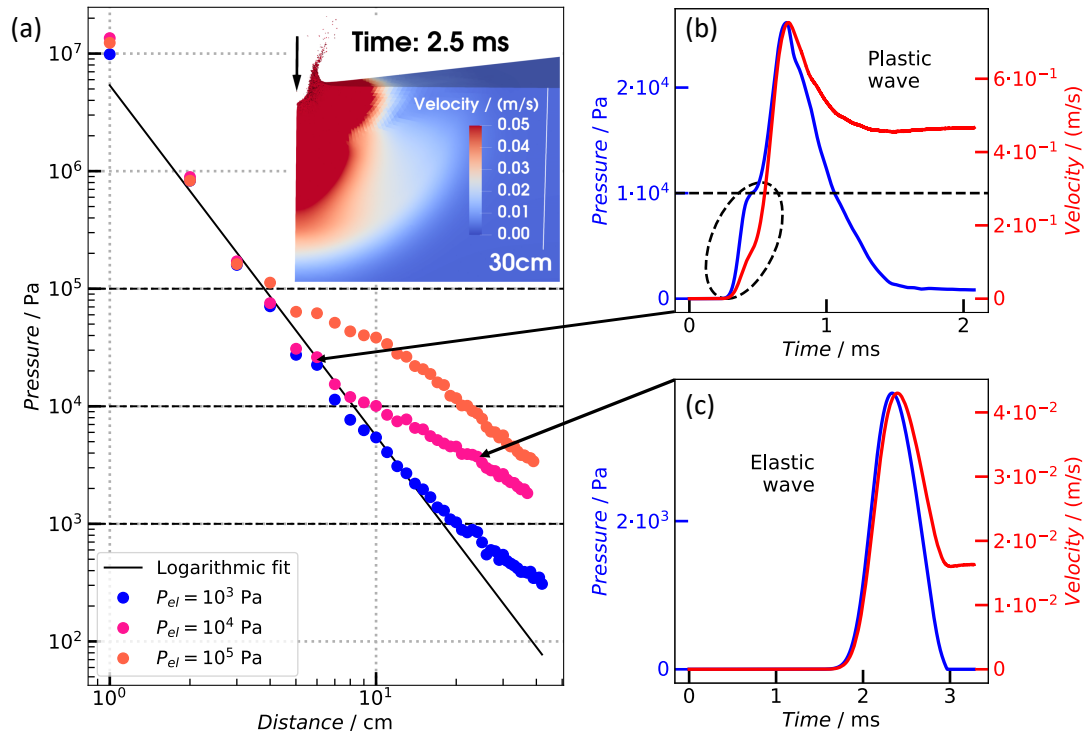


**Figure 2.** Evidence of an elastic and plastic regimes. (a) Shows the maximum modeled pressure recorded with distance for three different values of  $P_{el}$ . In inset, a snapshot of a HOSS simulation of the 0.98 km/s shot, showing the amplitude of the velocity and the ejected sand elements 2.5ms after the impact. (b) Waveform in an area where  $P$  exceeds  $P_{el} = 10^4$  Pa. The dashed circle indicates the elastic precursor followed by the plastic wave. (c) Waveform in an area further away from the impact with only an elastic wave.  $P_{el}$  appears to be an important parameter controlling the transition between these two regimes.

159 In a first test,  $P_{S_{max}}$  has been varied between  $10^6$  Pa down to  $10^3$  Pa. For  $P_{S_{max}} >$   
160  $10^5$  Pa, the seismic waves show no visible change of amplitude, shape or velocity away  
161 from the impactor. Indeed, the stress values reached with these low-energy impacts are  
162 typically around  $10^4$  Pa. Only a few elements within 5cm of the impact undergo pres-  
163 sures higher than  $10^6$  Pa. Therefore, the yield strength has to be lowered to very low val-  
164 ues of  $10^4$  or  $10^3$  Pa to produce a visible effect on the shock wave away from the source.  
165 These values are far from typical values of yield strength measured for sand (Berney IV  
166 & Smith, 2008) and can be considered unphysical, therefore the plastic wave is essen-  
167 tially unaffected by realistic yield strengths.

168 Consequently, we focus on the transition between elastic and plastic domain. It is  
169 known in shock physics that a deflection in the Shock-Hugoniot curve at the onset of plas-  
170 ticity results in the generation of two waves: the elastic precursor, which travels at elas-  
171 tic speed in the medium, and a plastic wave with slower propagation velocity and higher  
172 attenuation. These features are generated by the elastic-plastic transition in the EOS  
173 model, if  $K_{trans} < K_{el}$ . This change of regime is evident on Figure 2 as a change of  
174 the slope of the evolution of the maximum pressure with distance. The break corresponds  
175 to the distance at which the maximum pressure falls below  $P_{el}$ . Modeled signals for which  
176 the pressure exceeds  $P_{el}$  show an elastic precursor followed by a plastic wave, but con-  
177 tain only an elastic wave in the other case.

178 Table 1 gathers a series of measures on the effect of  $K_{el}$  and  $K_{trans}$  on the impact  
179 shock wave. Four experiments were ran with  $K_{el} = G = 10$  MPa and  $K_{trans}$  varying  
180 between  $\sim 1$  and  $\sim 8$  MPa. The velocity of the generated elastic wave was measured  
181 by picking the acceleration arrival times. As  $K_{el} > K_{trans}$ , a plastic wave is also cre-  
182 ated, whose move-out velocity can be computed using the peak time of the pressure wave  
183 between sensors placed every 1cm. For our value of bulk modulus  $K_{el}$  and shear mod-  
184 ulus  $G$ , the velocity of a purely acoustic wave is  $v_{acoustic} = \sqrt{\frac{K_{el}}{\rho}} = 107$  m/s, and  
185 the velocity of a solid P-wave is  $v_{solid} = \sqrt{\frac{K_{el} + \frac{4}{3}G}{\rho}} = 162$  m/s. The measured elastic-  
186 wave velocity in the granular material is  $v_{acoustic} < 133$  m/s  $< v_{solid}$ . Results show  
187 that the plastic wave itself propagates with a velocity slightly above  $\sqrt{\frac{K_{trans}}{\rho}}$ , but still  
188 slower than the measured elastic wave velocity. It also appears that, at a specific point  
189 in the tank, the ratio of pressure amplitude with the square root of  $K_{trans}$  has a sim-

**Table 1.** Parametric study of  $K_{trans}$  (Runs 1 to 4) and  $m$  (Runs 5 to 8). Plastic wave velocities have been measured by recording the time at which pressure peaks as a function of range. Elastic wave velocities have been measured by picking the acceleration wave arrival time with a threshold as a function of range. The theoretical value for this elastic wave velocity is between 107 and 162 m/s, as explained below. Peak pressure is also given at 20cm.

Run	$m$	$K_{trans}$ (MPa)	$\sqrt{\frac{K_{trans}}{\rho}}$ (m/s)	Plastic wave velocity (m/s)	Elastic wave velocity (m/s)	Peak pressure at 20cm (kPa)
1	5	7.9	95	$94 \pm 1$	$135 \pm 1$	5.15
2	5	4.9	75	$78 \pm 1$	$133 \pm 1$	2.54
3	5	2.8	58	$61 \pm 1$	$134 \pm 2$	1.57
4	5	0.9	34	$42 \pm 1$	$138 \pm 2$	0.85
5	6	1.5	40	$51 \pm 1$	$133 \pm 2$	1.01
6	5	1.5	40	$47 \pm 1$	$134 \pm 2$	1.01
7	4	1.5	40	$45 \pm 1$	$135 \pm 1$	0.97
8	3	1.5	40	$39 \pm 1$	$136 \pm 1$	0.87

190 ilar value for each experiment, suggesting a good agreement with a rough linear Hugo-  
191 not model of  $P \sim V_{impact} \sqrt{K\rho}$ .

192 To further analyse the effect of the pore-crush regime, the exponent  $m$  of the pore-  
193 crush curve is varied between 3 and 6, while the parameter  $K_{trans}$  is fixed to a value of  
194 1.5 MPa, and we repeat the same measurement as before. In Table 1, our results show  
195 that, at the scale of these experiments,  $m$  has only a moderate influence on the plastic  
196 wave velocity, as well as on the amplitude of the generated wave.

### 197 3.2 Volumetric Response of Pumice Sand

198 From the parametric study reported previously, it is possible to infer appropriate  
199 parameters to fit the experimental signals. To match the wave velocity measured on the  
200 vertical accelerometers of the AVGR shot,  $K_{el}$  is set to 10 MPa. The elastic precursor  
201 being visible up to 42cm below the impact point in the experiments,  $P_{el}$  must be lower  
202 than the maximum pressure reached at this point, which leads to  $P_{el} = 1\text{kPa}$ . To match  
203 the amplitudes of the wave on each of the sensors,  $K_{trans}$  is set to 6 MPa. The exper-  
204 imental data could not provide enough constraints on  $m$  or the parameters from the SE.  
205 We thus set the exponent  $m$  to 5, a number found in some high-pressure experiments  
206 in several types of sands (Yamamuro et al., 1996, 2011; Luo et al., 2011). The SE yield  
207 point is set to a value of 1 MPa, too high to create any visible yield in our sand, and the

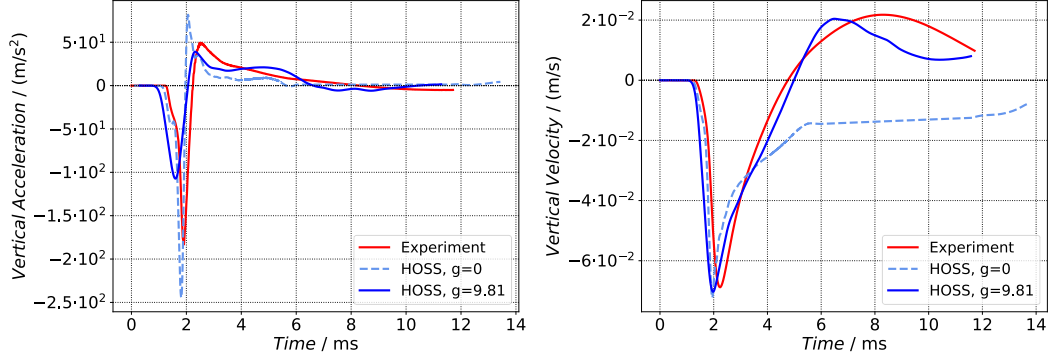


**Figure 3.** Compared numerical and experimental vertical acceleration (left) and velocity (right) signals for the 0.98 km/s impact velocity shot, recorded at a sensor 21cm directly below the impact point. The solid blue line and the dashed light-blue line correspond to simulations performed with and without earth gravity, respectively. The simulation better matches the experiment when gravity is considered.

208 friction coefficient is kept at 0.75. To study the effects of gravity on the results, we in-  
 209 clude an initial acceleration of  $-9.81 \text{ m/s}^2$  to one simulation, letting the sand relax to an  
 210 equilibrium over a few 100ms before the impact. Another simulation is run without grav-  
 211 ity, but both use the same material model parameters as listed above. The resulting nu-  
 212 merical and experimental waveforms are compared 21cm directly below the impact point  
 213 on Figure 3 and 30cm horizontally from the impact point on Figure 4, both with and  
 214 without the gravitational constraint.

215 On Figures 3 and 4, the modeled acceleration wave has an amplitude 40% lower  
 216 and 33% higher than the experimental signal for the vertical sensor with and without  
 217 gravity, respectively; and up to 100% higher for the horizontal sensor with no gravity.  
 218 The velocity wave, however, ranges closer to the experimental signal. The arrival times  
 219 at the vertical sensors match each other, in accordance with a measured vertical move-  
 220 out velocity of 150 m/s. For the shallow sensors, we measure a horizontal move-out ve-  
 221 locity closer to 80 m/s, while the modeled waves keep the same move-out velocity as for  
 222 the vertical sensors, thus being ahead of time.

## 223 4 Discussion, Conclusions and Future Work

224 The presence of gravity improves significantly the modeled material response to the  
 225 main shock. In the model without gravity, this response is weak enough so that the ve-  
 226 locity of the vertical sensor remains negative after 5ms (Figure 3). On the shallow sen-

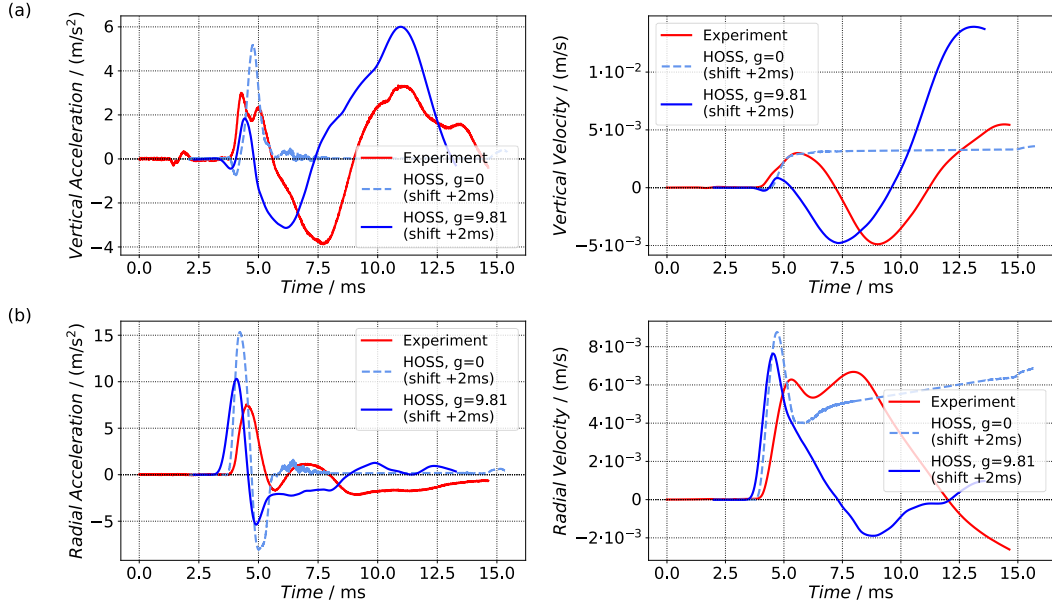


**Figure 4.** Compared numerical and experimental vertical (a) and radial (b) signals for the 0.98 km/s impact velocity shot. Both accelerations and velocities are shown for the sensor 30 cm radially away from the impact point. The solid blue line and the dashed light-blue line correspond to simulations performed with and without earth gravity, respectively. Note that modeled signals have been shifted in time to obtain a better match (see text for details).

227 sor, the modeled velocity reaches a constant positive value after 4ms when the acceler-  
 228 ation vanishes (Figure 4). This indicates that the element attached to this sensor is in  
 229 a non-accelerated motion, a "free-flight". The modeled signal with Earth gravity differ  
 230 greatly. On Figure 3, we can see that the counter-response of the material to the impact  
 231 is now strong enough to create a positive velocity on the vertical sensor, reproducing the  
 232 behavior of pumice sand of the experiment. Acceleration on the shallow sensor displayed  
 233 on Figure 4 doesn't show any longer evidence of free-flight but starts a cycle of falling  
 234 down and rebounding as seen on the experimental data.

235 The parametric study suggests that the plastic yield,  $P_{S_{max}}$ , has little influence on  
 236 the shock wave. This is due to the fact that the stress level in our modeling reaches at  
 237 most the order of 10 kPa, way lower than any documented plastic yield. The modeled  
 238 material thus remains in a regime where the SE can be approximated by a simple Mohr-  
 239 Coulomb surface. On the contrary, some questions remain on the effect of the elastic shear  
 240 modulus  $G$  of the material. In this study,  $G$ , which affects both the shear wave and Rayleigh  
 241 wave speed of an elastic material, was fixed once it became clear that the main shock

242 is mostly driven by the EOS parameters, but shear- or Rayleigh waves might still be an  
243 explanation for the late-time discrepancies between the modeled and experimental waves  
244 that are not caused by gravity. Moreover, this study shows that the wave move-out ve-  
245 locity is not completely determined by the elastic bulk modulus  $K_{el}$ , but rather lies be-  
246 tween the expected speed of sound in a fluid  $v_{acoustic}$  and the P-wave velocity in a solid  
247  $v_{solid}$ . A more thorough study of the influence of  $G$  could shed some light on the elas-  
248 tic speed of waves in granular media, which can neither be considered as a fluid nor as  
249 a traditional elastic solid, and will help calibrating the model with respect to the exper-  
250 iments.

251 The study of the pore-crush curve suggests that plastic processes in sand, such as  
252 pore collapse and grain displacement are particularly efficient in the shock attenuation,  
253 and that the slope of the pore-crush curve of the EOS is key in capturing this attenu-  
254 ation. Still, trade-offs exist between the model parameters analyzed. For example, pa-  
255 rameters  $K_{trans}$  and  $m$ , that define the pore-crush curve, play a role in the amplitude  
256 and peak time of the plastic wave. An increase in  $m$  could thus compensate for a decrease  
257 in  $K_{trans}$ . The low pressure part of the curve is easier to constrain with the available data,  
258 but the scale of the experiments does not allow for a proper determination of the high-  
259 pressure response. The high-pressure EOS and SE will be of higher importance in the  
260 case of real planetary impacts, where the energy involved is several orders of magnitude  
261 higher. For example, the impact velocity distributions computed for Mars from observed  
262 asteroid populations yield a mean impact velocity of 9.6 km/s (Ivanov, 2001). For bet-  
263 ter model accuracy at high pressures, other types of high-stress laboratory data or the-  
264 oretical models should be considered in the future.

265 In conclusion, the final model captures the vertical wave's shape and amplitude for  
266 an impact velocity of 0.98 km/s. This proves that HOSS can reproduce the main char-  
267 acteristics of an impact shock wave in granular media. The results have shown to be more  
268 sensitive to variations on the EOS parameters than to variation on the SE parameters.  
269 Gravity has proved to be a key parameter in the later stages of wave simulation by pro-  
270 viding a more realistic material response. However, the arrival times and amplitudes recorded  
271 at the shallow sensors cannot be reproduced by this model. Understanding this discrep-  
272 ancy requires further study, as a non-spherical wavefront needs to be modeled. Future  
273 works will investigate the effect of shear waves on the signal and the hypothesis of depth-  
274 dependant elastic properties created by the constraint of sand by gravity, as it has al-

275 ready been reported in literature (Morgan et al., 2018; van den Wildenberg et al., 2013).  
276 This non linear constraint creates a dependance of the bulk modulus with pressure in  
277 the elastic domain. Improving the fidelity of HOSS’ model to the experimental truth will  
278 bring more insight into the physics of shocks in granular, highly porous media and a new  
279 definition of equivalent seismic sources for impacts. Such new validated modeling capa-  
280 bility will help predict the signal of small planetary impacts, for which surface porous  
281 regolith endures most of the shock. These small impact might be recorded by InSight,  
282 if close enough, and provide new information on the crustal seismic properties of Mars.

### 283 **Acknowledgments**

284 This work is InSight contribution number 119 and LA-UR-19-32642. We thank the LANL-  
285 HPC environment for providing and maintaining the Los Alamos High-Performance Com-  
286 puting facilities and the NASA/AVGR facility for conducting the impact experiments.  
287 We also thank the reviewers whose comments helped improve and clarify this manuscript.  
288 Experimental data are in the process of being transferred to an online repository. More  
289 details on the parametric study can be found in the Master thesis of the author (Froment,  
290 2020). This work is funded by the LANL Center for Space and Earth Science (CSES)  
291 project XWPB00 and the ARPE student program of the École Normale Supérieure Paris-  
292 Saclay. The French co-authors are acknowledging the support of CNES and ANR (un-  
293 der contract MAGIS ANR-19-CE31-0008-08).

### 294 **References**

- 295 Allen, C. C., Morris, R. V., Lindstrom, D. J., Lindstrom, M., & Lockwood, J.  
296 (1997). JSC Mars-1-Martian regolith simulant. In *Proceedings of the*  
297 *28th lunar and planetary science conference*. Retrieved from [https://](https://www.lpi.usra.edu/meetings/lpsc97/pdf/1797.PDF)  
298 [www.lpi.usra.edu/meetings/lpsc97/pdf/1797.PDF](https://www.lpi.usra.edu/meetings/lpsc97/pdf/1797.PDF)
- 299 Banerdt, W. B., Smrekar, S. E., Banfield, D., Giardini, D., Golombek, M., Johnson,  
300 C. L., ... Wieczorek, M. (2020). Initial results from the InSight mission on  
301 Mars. *Nature Geoscience*. doi: <https://doi.org/10.1038/s41561-020-0544-y>
- 302 Banfield, D., Rodriguez-Manfredi, J. A., Russell, C. T., Rowe, K. M., Leneman, D.,  
303 Lai, H. R., ... Banerdt, W. B. (2019). InSight Auxiliary Payload Sensor Suite  
304 (APSS). *Space Science Reviews*, 215(1), 4.
- 305 Berney IV, E. S., & Smith, D. M. (2008). *Mechanical and Physical Properties of*  
306 *ASTM C33 Sand* (Tech. Rep.). US Army Engineer Research and Development  
307 Center, Geotechnical and Structures Laboratory.
- 308 Carrier, W. D., Olhoeft, G. R., & Mendell, W. (1991). Physical properties of the lu-  
309 nar surface. *Lunar sourcebook*, 475–594.
- 310 Collins, G. S., Housen, K. R., Jutzi, M., & Nakamura, A. M. (2019). Planetary  
311 impact processes in porous materials. In *Shock phenomena in granular and*  
312 *porous materials* (pp. 103–136). Springer.
- 313 Daubar, I., Lognonné, P., Teanby, N. A., Miljkovic, K., Stevanović, J., Vaubailon,

- 314 J., ... Banerdt, B. W. (2018). Impact-seismic investigations of the InSight  
315 mission. *Space Science Reviews*, 214(8), 132.
- 316 Daubar, I., McEwen, A. S., Byrne, S., Kennedy, M., & Ivanov, B. (2013). The cur-  
317 rent martian cratering rate. *Icarus*, 225(1), 506–516.
- 318 Froment, M. (2020). Internship Report: Numerical modelling of impact seismic sig-  
319 nals on regolith. *Office of Scientific and Technical Information*. doi: <https://doi.org/10.2172/1593106>
- 320
- 321 Gao, K., Guyer, R., Rougier, E., Ren, C. X., & Johnson, P. A. (2019). From stress  
322 chains to acoustic emission. *Physical review letters*, 123(4), 048003.
- 323 Giardini, D., Lognonné, P., Banerdt, W. B., Pike, W. T., Christensen, U., Ceylan,  
324 S., ... Yana, C. (2020). The seismicity of Mars. *Nature Geoscience*. doi:  
325 <https://doi.org/10.1038/s41561-020-0539-8>
- 326 Guldemeister, N., & Wünnemann, K. (2017). Quantitative analysis of impact-  
327 induced seismic signals by numerical modeling. *Icarus*, 296, 15 - 27.
- 328 Hapke, B., & van Hoen, H. (1963). Photometric studies of complex surfaces, with  
329 applications to the moon. *Journal of Geophysical Research*, 68(15), 4545–  
330 4570.
- 331 Hyodo, M., Hyde, A. F., Aramaki, N., & Nakata, Y. (2002). Undrained monotonic  
332 and cyclic shear behaviour of sand under low and high confining stresses. *Soils  
333 and Foundations*, 42(3), 63–76.
- 334 Ivanov, B. A. (2001). Mars/Moon cratering rate ratio estimates. *Space Science Re-  
335 views*, 96(1-4), 87–104.
- 336 Lei, Z., Rougier, E., Knight, E., & Munjiza, A. (2014). A framework for grand scale  
337 parallelization of the combined finite discrete element method in 2d. *Computa-  
338 tional Particle Mechanics*, 1(3), 307–319.
- 339 Lei, Z., Rougier, E., Knight, E. E., Frash, L., Carey, J. W., & Viswanathan, H.  
340 (2016). A non-locking composite tetrahedron element for the combined finite  
341 discrete element method. *Engineering Computations*.
- 342 Lei, Z., Rougier, E., Knight, E. E., Munjiza, A., & Viswanathan, H. (2016). A gen-  
343 eralized anisotropic deformation formulation for geomaterials. *Computational  
344 Particle Mechanics*, 3(2), 215–228.
- 345 Lognonné, P., Banerdt, W., Pike, W., Giardini, D., Christensen, U., Garcia, R.,  
346 ... Zweifel, P. (2020). Constraints on the shallow elastic and anelas-  
347 tic structure of Mars from InSight seismic data. *Nature geoscience*. doi:  
348 <http://doi.org/10.1038/s41561-020-0536-y>
- 349 Lognonné, P., Banerdt, W. B., Giardini, D., Pike, W. T., Christensen, U., Laudet,  
350 P., ... Wookey, J. (2019). SEIS: Insight’s Seismic Experiment for Internal  
351 Structure of Mars. *Space Science Reviews*, 215(1), 12.
- 352 Lognonné, P., & Johnson, C. L. (2007). Planetary seismology. *Treatise on Geo-  
353 physics*, 10, 69–122.
- 354 Luo, H., Lu, H., Cooper, W. L., & Komanduri, R. (2011). Effect of mass density on  
355 the compressive behavior of dry sand under confinement at high strain rates.  
356 *Experimental mechanics*, 51(9), 1499–1510.
- 357 Malin, M. C., Edgett, K. S., Posiolova, L. V., McColley, S. M., & Dobrea, E. Z. N.  
358 (2006). Present-day impact cratering rate and contemporary gully activity on  
359 mars. *science*, 314(5805), 1573–1577.
- 360 Morgan, P., Grott, M., Knapmeyer-Endrun, B., Golombek, M., Delage, P.,  
361 Lognonné, P., ... Kedar, S. (2018). A pre-landing assessment of regolith  
362 properties at the InSight landing site. *Space Science Reviews*, 214(6), 104.
- 363 Munjiza, A. (2004). *The combined finite-discrete element method*. John Wiley &  
364 Sons.
- 365 Munjiza, A., Knight, E. E., & Rougier, E. (2011). *Computational mechanics of dis-  
366 continua*. John Wiley & Sons.
- 367 Munjiza, A., Knight, E. E., & Rougier, E. (2014). *Large Strain Finite Element  
368 Method: A Practical Course*. John Wiley & Sons.

- 369 Munjiza, A., Rougier, E., Knight, E. E., & Lei, Z. (2013). HOSS: An integrated  
370 platform for discontinua simulations. In G. Chen, Y. Ohnishi, L. Zheng, &  
371 T. Sasaki (Eds.), *Frontiers of discontinuous numerical methods and practical*  
372 *simulations in engineering and disaster prevention* (pp. 97–104). CRC Press.  
373 Retrieved from <https://doi.org/10.1201/b15791-12>
- 374 Pierazzo, E., Artemieva, N., Asphaug, E., Baldwin, E. C., Cazamias, J., Coker, R.,  
375 ... Wünnemann, K. (2008). Validation of numerical codes for impact and  
376 explosion cratering: Impacts on strengthless and metal targets. *Meteoritics &*  
377 *Planetary Science*, *43*(12), 1917-1938.
- 378 Richardson, J., & Kedar, S. (2013). An experimental investigation of the seismic sig-  
379 nal produced by hypervelocity impacts. In *Lunar and planetary science confer-*  
380 *ence* (Vol. 44, p. 2863).
- 381 Sun, Q., Wang, G., & Hu, K. (2009, 05). Some open problems in granular matter  
382 mechanics. *Progress in Natural Science - PROG NAT SCI*, *19*. doi: 10.1016/  
383 j.pnsc.2008.06.023
- 384 Teanby, N. (2015). Predicted detection rates of regional-scale meteorite impacts on  
385 Mars with the InSight short-period seismometer. *Icarus*, *256*, 49–62.
- 386 van den Wildenberg, S., van Loo, R., & van Hecke, M. (2013). Shock waves in  
387 weakly compressed granular media. *Physical review letters*, *111*(21), 218003.
- 388 Wünnemann, K., Collins, G., & Melosh, H. (2006). A strain-based porosity model  
389 for use in hydrocode simulations of impacts and implications for transient  
390 crater growth in porous targets. *Icarus*, *180*(2), 514–527.
- 391 Yamamuro, J. A., Abrantes, A. E., & Lade, P. V. (2011). Effect of strain rate on the  
392 stress-strain behavior of sand. *Journal of Geotechnical and Geoenvironmental*  
393 *Engineering*, *137*(12), 1169–1178.
- 394 Yamamuro, J. A., Bopp, P. A., & Lade, P. V. (1996). One-dimensional compression  
395 of sands at high pressures. *Journal of geotechnical engineering*, *122*(2), 147–  
396 154.